Journal of Biomedical Optics

BiomedicalOptics.SPIEDigitalLibrary.org

In vivo wide-field multispectral scanning laser ophthalmoscopy–optical coherence tomography mouse retinal imager: longitudinal imaging of ganglion cells, microglia, and Müller glia, and mapping of the mouse retinal and choroidal vasculature

Pengfei Zhang
Azhar Zam
Yifan Jian
Xinlei Wang
Yuanpei Li
Kit S. Lam
Marie E. Burns
Marinko V. Sarunic
Edward N. Pugh,, Jr.
Robert J. Zawadzki

SPIE.

In vivo wide-field multispectral scanning laser ophthalmoscopy–optical coherence tomography mouse retinal imager: longitudinal imaging of ganglion cells, microglia, and Müller glia, and mapping of the mouse retinal and choroidal vasculature

Pengfei Zhang,[a] Azhar Zam,[a] Yifan Jian,[d] Xinlei Wang,[a] Yuanpei Li,[b] Kit S. Lam,[b] Marie E. Burns,[a,c] Marinko V. Sarunic,[d] Edward N. Pugh, Jr.,[a] and Robert J. Zawadzki[a,c,*]

[a]University of California Davis, Department of Cell Biology and Human Anatomy, UC Davis RISE Eye-Pod Laboratory, 4320 Tupper Hall, Davis, California 95616, Unites States

[b]UC Davis Comprehensive Cancer Center, Department of Biochemistry and Molecular Medicine, 4501 X Street, Sacramento, California 95817, Unites States

[c]University of California Davis, UC Davis Eye Center, Department of Ophthalmology and Vision Science, 4860 Y Street, Suite 2400, Sacramento, California 95817, Unites States

[d]Simon Fraser University, School of Engineering Science, 8888 University Drive, Burnaby, British Columbia V5A 1S6, Canada

Abstract. Scanning laser ophthalmoscopy (SLO) and optical coherence tomography (OCT) provide complementary views of the retina, with the former collecting fluorescence data with good lateral but relatively low-axial resolution, and the latter collecting label-free backscattering data with comparable lateral but much higher axial resolution. To take maximal advantage of the information of both modalities in mouse retinal imaging, we have constructed a compact, four-channel, wide-field (~50 deg) system that simultaneously acquires and automatically coregisters three channels of confocal SLO and Fourier domain OCT data. The scanner control system allows "zoomed" imaging of a region of interest identified in a wide-field image, providing efficient digital sampling and localization of cellular resolution features in longitudinal imaging of individual mice. The SLO is equipped with a "flip-in" spectrometer that enables spectral "fingerprinting" of fluorochromes. Segmentation of retina layers and *en face* display facilitate spatial comparison of OCT data with SLO fluorescence patterns. We demonstrate that the system can be used to image an individual retinal ganglion cell over many months, to simultaneously image microglia and Müller glia expressing different fluorochromes, to characterize the distinctive spatial distributions and clearance times of circulating fluorochromes with different molecular sizes, and to produce unequivocal images of the heretofore uncharacterized mouse choroidal vasculature. [DOI: 10.1117/1.JBO.20.12.126005]

Keywords: scanning laser ophthalmoscopy; optical coherence tomography; multimodal imaging; mouse retinal imaging; fluorescent nanoparticles.

Paper 150478PRR received Jul. 15, 2015; accepted for publication Oct. 21, 2015; published online Dec. 16, 2015.

1 Introduction

The mouse is an important model organism in ophthalmic research. As a part of the brain, the retina offers a unique opportunity to directly visualize changes associated with neurodegenerative disorders and vascular alterations, and to assess therapeutic interventions.[1] To better visualize the cellular microstructure and understand the molecular processes in the living retina, high-resolution retinal imaging of rodent eyes is desirable. Recently, two kinds of noninvasive retinal imaging modalities, scanning laser ophthalmoscopy (SLO) and optical coherence tomography (OCT), have been successfully applied to monitor structural changes in the retinas of individual mice in longitudinal studies.[1–8] SLO is a common diagnostic imaging technique in ophthalmology[9,10] and can generate images from retinal reflectance, autofluorescence, and extrinsic fluorescence. At the same time, the confocal arrangement helps SLO reject scattered light and improve image contrast, and potentially achieve moderate depth sectioning. In addition, an SLO can detect signals from exogenous fluorescence agents, such as fluorescein and indocyanine green, to improve imaging contrast of retinal and choroidal vasculature. Applied to mice, SLO also affords the possibility of imaging of cell-specific fluorescent proteins, introduced into the eye either through genetic engineering or by viral-mediated gene transfer.

Fourier domain optical coherence tomography (Fd-OCT), which combines high axial resolution with high recording speed, is another very important retinal imaging modality.[11–14] OCT generates intrinsically volumetric data from the interference of low-coherence infrared light traversing the reference and sample arms. The light from the sample arm that reaches the OCT detector is the portion of the probing sample beam

*Address all correspondence to: Robert J. Zawadzki, E-mail: rjzawadzki@ucdavis.edu

that was backscattered from different layers in the imaged tissue. This backscattered light interferes with that of the reference arm light, and the resulting interferometric signal is recorded in the Fourier domain by a spectrometer, resulting in parallel mapping of the relative reflectance of different retinal layers. The lateral resolution achieved with OCT systems for retinal imaging is comparable to that obtained with SLO, but the depth resolution, which is determined by the bandwidth of the broadband light source, is much better (typically, a few micrometers).[15]

The multimodal imaging system presented here was specifically designed and built for *in vivo* mouse retinal imaging and integrates SLO, OCT, and a fluorescence emission spectrometer. Each optical modality implemented in the system has its own advantages and limitations. By combining them, the multimodal system simultaneously collects the complementary information from the tissue of the different modalities, greatly simplifying data registration and analysis.[5,16–23] With its customized scanning head, the scanning field of view (FOV) can be up to 50 deg, while software control allows limiting the scanning to any square subfield of the larger field. With a customized contact lens mounted to the scan head, the mouse cornea can be easily kept hydrated and clear for an hour or more, greatly facilitating performance of complex experiments during a single imaging session.

2 Methods

2.1 *System Hardware*

The combined SLO and OCT imaging platform was custom designed for imaging the retina of the adult mouse eye, which has a diameter of ~3.2 mm and a posterior nodal distance of ~2 mm.[24] Its core optics are compactly arranged in an $8'' \times 8''$ frame and sit on a platform that can be easily tilted and translated, providing precision alignment with respect to the eye of the anesthetized mouse. A heating pad was used to maintain the mouse's normal body temperature and avoid the development of "cold cataracts" during imaging. The mouse's head was held rigidly by a "bite-bar" that also served to keep its snout inside the gaseous isoflurane anesthetic delivery tube.[25]

2.1.1 *Scanning laser ophthalmoscopy subsystem*

As shown in Fig. 1(a), a super-continuum laser (SC-400 Fianium, Southampton, U.K.) is used as the light source for the SLO subsystem. By changing bandpass filter 1, different excitation wavelengths can be chosen. Currently, a dual-band bandpass filter (FF01-482/563, Semrock, Rochester, NY) is placed in the laser beam to restrict the light source spectrum to two spectral bands, providing strong excitation for green fluorescent protein (GFP) and mCherry, respectively, delivering a total of 250 μW at the mouse pupil. A single bandpass filter (MF469-35, Thorlabs, Newton, NJ) delivering 200 μW was used if only GFP-band excitation was desired. Emitted fluorescent light was separated by a dichroic mirror, DM1 (Di01-R488/561, Semrock, Rochester, NY) and collected by two photomultiplier modules, PMT2 and PMT3 (H7422-40 and H7422-50, respectively; Hamamatsu, Nagoya, Japan). Bandpass filters 2 and 3 (FF01-525/45 and FF01-609/54, Semrock, Rochester, NY) were used to further restrict the emission bands collected by PMT2 and PMT3 for GFP and mCherry, respectively. A reflected light signal was acquired by PMT1 (H7422-20 Hamamatsu, Nagoya, Japan). By flipping mirror M1 in and out of the beam, the light can be directed into spectrometer2 (QE65000 Ocean optics, Dunedin, New Zealand) to measure the fluorescence emission spectrum; when operating in spectrometer mode, the SLO can operate either in "point excitation" (no scanning) or "region of interest (ROI)" (scanning) mode, though the recorded spectral information in the latter mode arises from the entire ROI. A photo of a mouse positioned for imaging is shown in Fig. 1(b).

2.1.2 *Optical coherence tomography subsystem*

The Fd-OCT system imaging beam was optically connected to the SLO subsystem via the second dichroic mirror (DM2). The OCT used a broadband light source (Broadlighter 890, Superlum, Carrigtohill, Ireland) with a 132-nm bandwidth centered at 860 nm, and delivered 600 μW at the mouse pupil plane, which provides ~2-μm theoretical axial resolution in tissue. A custom spectrometer (spectrometer1) with a high-speed line CMOS camera (Sprint spL4096-140 km, Basler, Ahrensburg, Germany) was used as the OCT detector. The OCT system operates at speeds up to 125,000 A-scan/s.[26] The OCT system can be operated in standard and phase-variance OCT (pv-OCT) acquisition modes; in the latter mode, several B-scans are acquired consecutively at the same position.[27–29] pv-OCT is one of several recently introduced OCT angiography (OCTA) methods

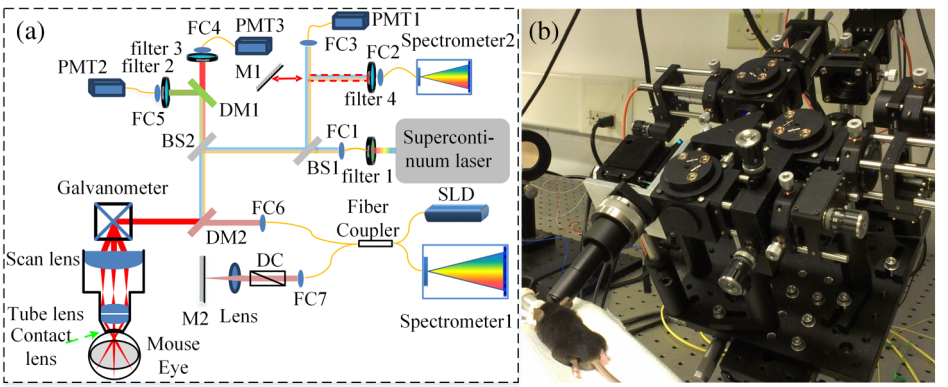

Fig. 1 Multispectral combined scanning laser ophthalmoscopy (SLO) and optical coherence tomography (OCT) imaging system. (a) Schematic—BS: beam splitter; DM: dichroic mirror; DC: dispersion compensation; FC: fiber collimator; SLD: super-luminescent diode; PMT: photomultiplier tubes. (b) Photo of mouse positioned for imaging. The mouse's incisures are hooked over a small "bite-bar," and its snout is held in a tube that delivers oxygen and isoflurane anesthetic.

allowing contrast agent-free visualization of blood flow, and mapping of the vasculature.[30–38]

2.1.3 *Contact lens*

A zero diopter mouse contact lens (0 Dpt., 1.65-mm radius of curvature with 2.5 mm diameter, Unicon Corporation, Osaka, Japan) was used to keep the mouse cornea hydrated. The contact lens was physically mounted on the imaging system scanning head and serves as the primary refractive element in imaging the retina. This allowed fixing its position with respect to the SLO/OCT system imaging optics and resulted in removing variation in retinal image quality caused by variable contact lens placement. With this approach, it is easier to keep the outer surface of the contact lens clean and—given that the mouse's head is rested on a bite-bar embedded in the isoflurane delivery system—to maintain stable and highly reproducible imaging for periods of an hour or more.

2.2 *Imaging System Performance*

As the SLO and OCT subsystems share the same scanning optics, they have the same scanning FOV, greatly facilitating coregistration of the data of the two imaging modalities. In our previous paper, the SLO subsystem's lateral resolution was calibrated.[39] Thus, the lateral resolution of the OCT subsystem can be estimated by taking into consideration the center wavelength difference, whereas the axial resolution can be calculated according to the light source bandwidth and center wavelength with standard formulas. The key parameters of the combined system are given in Table 1. The beam diameters at mouse pupil for both the OCT and SLO were set to 0.4 mm (pupil diameter is 2 mm typically) to reduce the influence of monochromatic aberrations and obtain diffraction-limited images. Effects of chromatic aberrations in the mouse eye are similar to the ones observed in the human eye.[40] Longitudinal chromatic aberrations were corrected by adjusting divergence of both OCT and SLO imaging beams to focus on the same depth. Any remaining effect of transverse chromatic aberrations was corrected by coregistering images acquired by two different wavelengths using imageJ StackReg function.[41]

2.3 *Mouse Handling*

2.3.1 *Mouse strains and husbandry*

All mouse husbandry and handling including imaging were in accordance with an animal study protocol approved by the University of California Animal Care and Use Committee, which is accredited by Association for Assessment and Accreditation of Laboratory Animal Care International and strictly adhere to all the National Institutes of Health (NIH) guidelines. All mice imaged in the study were obtained from Jackson Labs or bred in our colony, including pigmented (C57BL/6J) mice, albino (Balb/c or NU/NU) mice, and mice expressing fluorescent proteins in specific retinal cell types (microglia: $Cx3cr1^{GFP/+}$, $Cx3cr1^{GFP/GFP}$; sparse subset of retinal ganglion cells: *B6.Thy1-YFP-H*). Some of the mice studied had intraocular injections of an adeno-associated virus construct (AAV1/2-GFAP-mCherry) designed to drive expression of mCherry in retinal Müller glial cells.

2.3.2 *Anesthesia, pupil dilation, and corneal hydration*

During image acquisition, mice were anesthetized with the inhalational anesthetic isoflurane (2% in O_2). Pupils were dilated with tropicamide and phenylephrine, and the corneas kept hydrated by means of the contact lens (as described above) and a gel (Gel Tears, Chem-Pharm Fabrik, Berlin, Germany) that also served to largely neutralize refraction by the cornea, so that the contact lens was the primary refracting surface.

2.3.3 *Angiography*

Fluorescence angiography was performed with a mixture of two sterile fluorescent agents with well-separated excitation and emission spectra: fluorescein (ex 495 nm, em 520 nm; AK-Fluor, Akorn Pharmaceuticals, Lake Forest, IL) and rhodamine-X (ex 573 nm; em 592 nm; Thermo Fisher Scientific, Waltham). The rhodamine-X was conjugated to 30-nm-diameter micellar nanoparticles. The nanoparticles were synthesized from rhodamine-X-labeled telodendrimers via solution phase condensation reaction according to our reported methods.[42,43] The nanoparticles were then prepared via the self-assembly of telodendrimers in aqueous solution.[44] The concentrations of the two fluorochromes in PBS stock solutions were measured spectrophotometrically assuming extinction maxima of 83,000 and 129,000 $L\,mol^{-1}\,cm^{-1}$, respectively, for fluorescein and rhodamine-X. For imaging, a mixture of the two fluorochromes was made that had ~4 mM fluorescein and 200 μM rhodamine-X; 100 μL of this cocktail was injected into a tail vein for angiography. Assuming the blood volume of an adult mouse is ~1.5 mL, the concentrations in the mouse blood stream for the fluorochromes were 270 and 13 μM, respectively, for fluorescein and rhodamine-X.

3 Results

3.1 *Wide-Field Imaging with "Zoom-in" Capability Enables Long-Term Imaging of Single Retinal Neurons*

The "zoom-in" feature of our SLO scanning control system enables rapid location in the wide-field 50 deg FOV of an ROI for

Table 1 Key parameters of the SLO and OCT subsystems.

	Light source	Beam diameter in pupil plane	Axial resolution	Lateral resolution	Max point/ A-scan rate	Frame/ C-Scan rate	Lateral imaging range
SLO	Super-continuum (400 to 2400 nm)	0.4 mm	120 μm	~3 μm at 530 nm	500 kHz	2 Hz (256 × 256 pixels, 200 kHz point scan rate)	Up to ~50 deg (1.7 mm)
OCT	SLD (132 nm band centered at 860 nm)	0.4 mm	2 μm	~5 μm at 860 nm	125 kHz	0.2 Hz (1024 × 256 A-scans, 50 kHz A-scan rate)	Up to ~50 deg (1.7 mm)

higher digital-resolution imaging. Specifically, in the "zoom-in" mode, the full digital sampling (typically 256 × 256) is allocated to an ROI selected by drawing a box on a stored and displayed wide-field image. Figures 2(a) and 2(b) show *in vivo* wide-field reflection and fluorescence images, respectively, of a B6.Thy1-YFP-H transgenic mouse, whose retina has a sparse distribution of YFP-expressing ganglion cells.

During initial screening of this mouse, we noticed a large single ganglion cell with strong YFP fluorescence and performed zoomed-in scanning of a region of interest (ROI) [red rectangle box in Fig. 2(b)] enclosing the cell. In the zoomed view, the cell's axon and dendrites are clearly resolved. To evaluate the potential of our imaging platform for longitudinal studies, we imaged this same cell in a series of imaging sessions spanning 8 months. Figures 2(d) and 2(e) show images taken at 3 and 8 months, respectively, after the initial image. The superposition of these three images in a single RGB image [Fig. 2(f)] reveals that there are no major changes in the cell's morphology over this 8-month span. Subtle changes in morphology, such as that might occur with location-selective stimulation, should be readily detected with this approach. Wide-field imaging combined with zoom-in capability obviates the need for realignment for higher digital-resolution scanning and facilitates high-resolution imaging of the same retinal locus over the lifetime of an animal.

3.2 *Dual-Band Fluorescence Imaging Enables Spatial Relationships Between Different Cell Types to be Investigated*

To illustrate the multichannel imaging capability of our system performance, we imaged a $Cx3cr1^{GFP/+}$ mouse that had received an intravitreal injection of a viral construct (AAV1/2-GFAP-mCherry). This strain of mice constitutively expresses GFP in microglia cells and macrophages, while the viral construct drives the expression of the red fluorescent protein, mCherry, in Müller glial cells. Figures 3(a) and 3(b) are the wide-field SLO back-reflection and fluorescence image, respectively.

The inset, dashed rectangle, in Fig. 3(b) points out the location of the zoomed-in scan shown in Fig. 3(c). Using the spectrometer, we confirmed the emission spectra of GFP and mCherry acquired with the excitation beam focused on individual cells [Fig. 3(d)]. More generally, spectral analysis provides a means not only of distinguishing between strongly fluorescent exogenous fluorochromes but also of distinguishing weakly fluorescent exogenous fluorochromes from autofluorescence.[44]

3.3 *Simultaneous Scanning Laser Ophthalmoscopy and Optical Coherence Tomography Data Acquisition and Analysis Can Resolve Reflectance Anomalies*

In an initial test of our combined SLO/OCT system, we imaged homozygous $Cx3cr1^{GFP/GFP}$ mice, whose retinal microglial cells more strongly express GFP than heterozygous $Cx3cr1^{+/GFP}$ mice. During data acquisition, SLO and OCT scanning beams simultaneously raster across the retina with a 50-kHz point/A-scan rate. Since the SLO and OCT data are automatically coregistered, it is straightforward to generate simultaneous *en face* visualizations of both channels: Figure 4(a) shows the averaged wide-field SLO back-reflection image, while Fig. 4(b) shows an *en face* projection from the nerve fiber layer (NFL) of a single OCT volume. Averaging over 50 SLO scans [Fig. 4(a)]

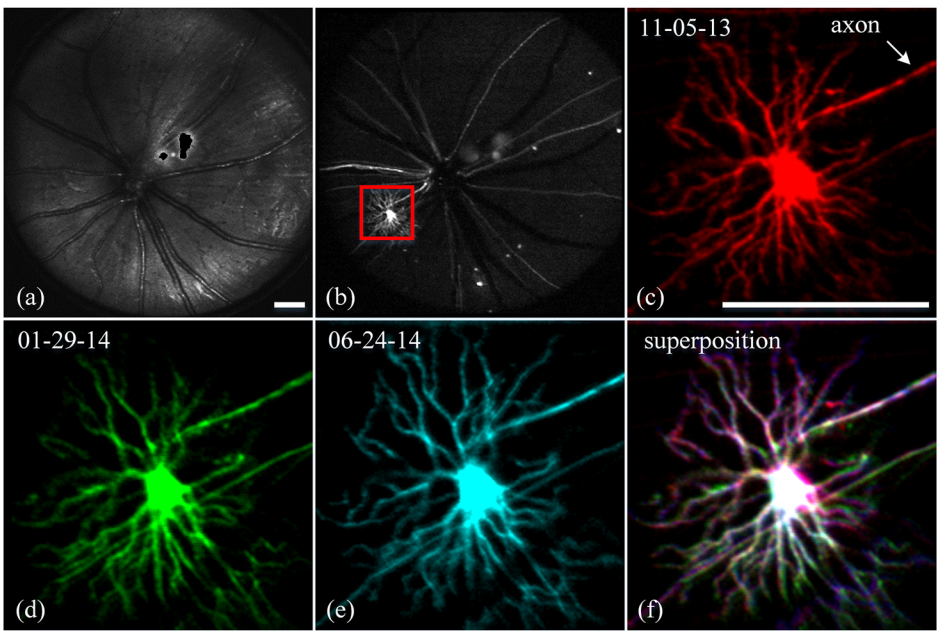

Fig. 2 Longitudinal imaging of a single retinal neuron (*B6.Thy1-YFP-H*): (a), (b) wide-field reflectance and fluorescence images, respectively; (c)–(e) single cell [marked in rectangle area in (b)] tracking in different days; (f) superposition image generated from (c) to (e). The images in (c)–(e) have been arbitrarily colorized for clarity, and in (f), the images were converted into R, G, B components and combined, after coregistration with the "affine" operator of Fiji ImageJ. (The variation in the color of the dendritic tree of the cell in panel (f) arises from small variations in the focal plane position between imaging sessions; the irregular black spot in panel (a) (and in subsequent figures) is used to mask a reflection artifact). Scale bar: 200 μm.

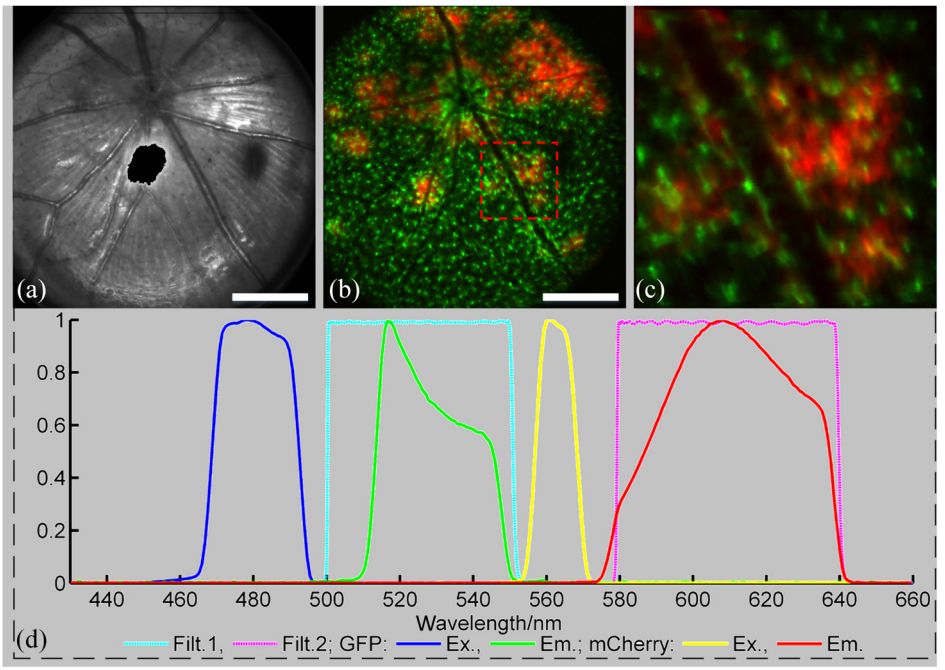

Fig. 3 Dual-fluorescence images of mouse retina with both EGFP-(microglia) and mCherry (Muller cell) expression: (a) SLO back-reflection wide-field image; (b) composite dual-channel fluorescence image acquired simultaneously with the reflectance image; (c) "zoom-in" fluorescence image of the red-rectangular ROI in (b); (d) measured exciting light distribution (Ex) and measured emission spectra (Em) from selected ROIs, along with the published spectral transmission spectra of the bandpass filters employed. Scale bar: 375 μm

suppressed the breathing artifacts [horizontal streaks in the OCT *en face* images in Figs. 4(b)–4(e)]. Figure 4(c) provides a color-coded display of the SLO back-reflection image (ocean blue) and the OCT NFL layer *en face* intensity projection (red). This display shows that the SLO and OCT images are automatically coregistered, and enables analysis of the origins of SLO and OCT signals from the same retinal areas. For example, we observed two apparent blood vessels in the SLO image that were absent from the OCT NFL layer projection [pointed by green arrows in Figs. 4(a) and 4(c)]. To resolve this discrepancy,

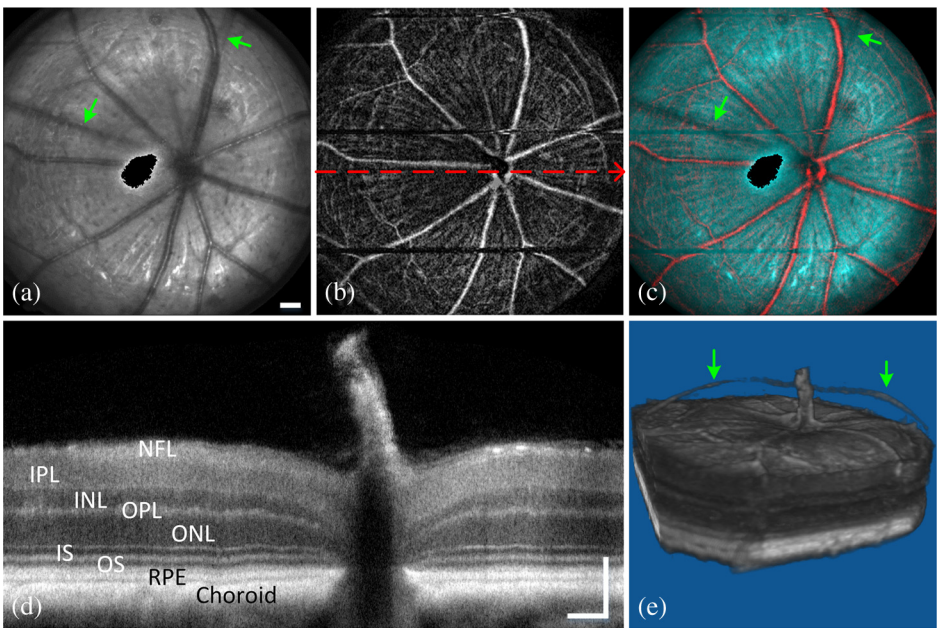

Fig. 4 Simultaneous SLO and OCT imaging of a *Cx3cr1*$^{GFP/GFP}$ mouse: (a) SLO back-reflection image; (b) OCT volume *en face* projection; (c) superposition of SLO (blue) and OCT NFL layer enface projection (red); (d) OCT B-scan along the red arrow in (b); retinal layers are labeled as follows: nerve fiber layer/retinal ganglion cell layer (NFL/RGCL), inner plexiform layer (IPL), inner nuclear layer (INL), outer plexiform layer (OPL), outer nuclear layer (ONL), photoreceptor inner segment/outer segment (IS/OS), and retinal pigment epithelium (RPE); (e) OCT volume display. Scale bar: 100 μm.

we reassessed the OCT data in a volume rendering. An example 3-D perspective projection view of the whole OCT volume is shown in Fig. 4(e) and revealed that these vessels were in fact located in the vitreous, probably due to an individual congenital abnormality in the retina of the mouse and not caused by *Cx3cr1* gene mutation in general. To illustrate the depth sectioning, in Fig. 4(d), we present an averaged B-scan ($n = 10$) taken along a meridian through the optic disc [red arrow in Fig. 4(b)]. Here, all the mouse retinal layers can be clearly resolved and are labeled by their conventional acronyms.

3.4 *Segmentation of Optical Coherence Tomography Images by Retinal Layer Reveals Novel Two-Dimensional Spatial Details*

OCT segmentation provides a means of better illustrating the advantage of the C-scan visualization of (volumetric) OCT data and its complementarity with SLO data.[45,46] To illustrate this, we imaged the Cx3cr1$^{GFP/GFP}$ mouse and manually segmented the OCT volumetric data based on changes in retina layer intensity using custom-written MATLAB code (MathWorks, Natick) and generated *en face* intensity projection views of different retinal layers. For orientation, in Fig. 5(a), we present one segmented B-scan. Nine distinct retinal layers were resolved, and Figs. 5(b)–5(f) show their *en face* intensity projections.

In Fig. 5(b), one can see the optic nerve head, major retinal arteries and veins, as well as axon bundles of retinal ganglion cells radially projecting to the optic nerve head. Comparison of Figs. 5(c) and 5(d) clearly reveals the differences between morphology of the microcapillary beds of the IPL and OPL layers as characterized by histology and OCTA.[47,48] Figure 5(e) shows the averaged intensity projection in the vicinity of the external limiting membrane (ELM) and highlights a pattern of highly scattering spots, which are not seen in wild type (WT) controls (data not shown). We explored the possibility that the hyper-reflecting spots had a corresponding signature in the fluorescence channel [Fig. 5(g)]. While some of the hyper-reflecting structures within ELM seem to be colocalized with most hyper-fluorescent spots, we feel that no obvious spatial correlation between the location of the microglia and the scattering spots exists [Fig. 5(h)]. Since hyper-reflecting spots in the ELM are not observed in normal healthy retinas, they probably represent some local pathology. Microglia cells are the resident macrophages in the retina and thus as the immune defense cells are constantly scavenging

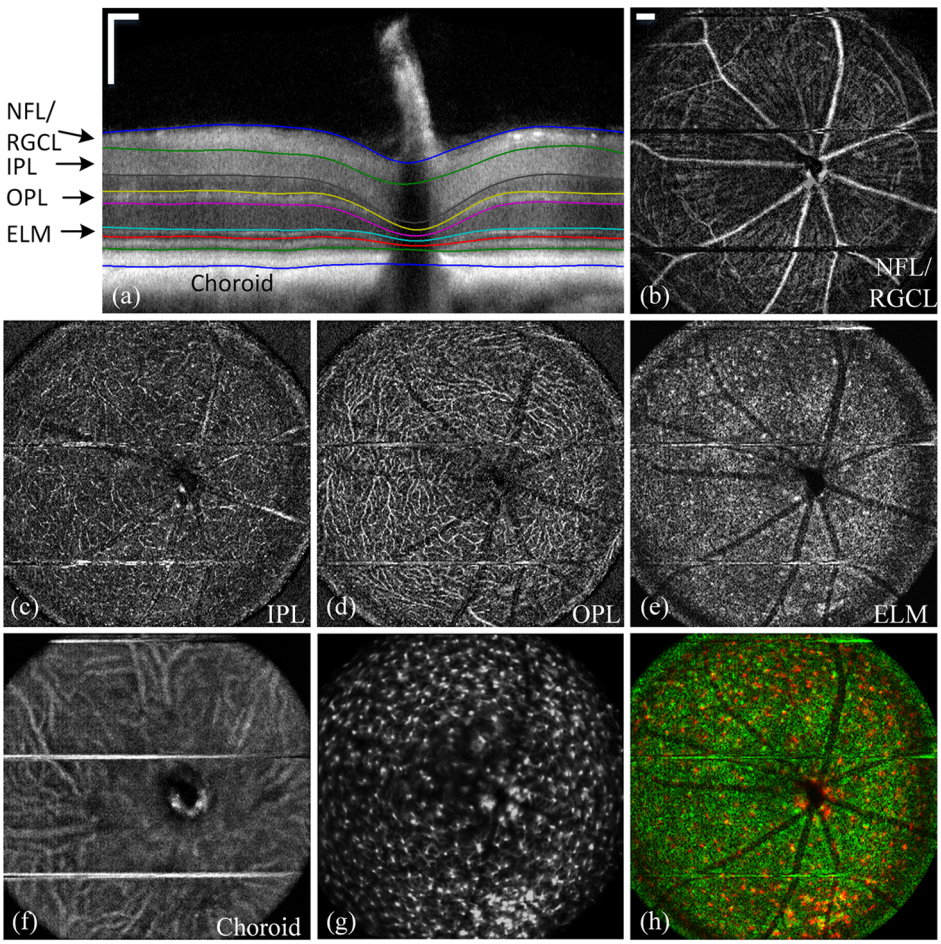

Fig. 5 OCT *en face* intensity projection and SLO fluorescence images from a Cx3cr1$^{GFP/GFP}$ mouse: (a) B-scan through the optic disc showing the segmentation boundaries; retinal layers are labeled as follows: nerve fiber layer/retinal ganglion cell layer (NFL/RGCL), inner plexiform layer (IPL), outer plexiform layer (OPL), and the layers around external limiting membrane (ELM); (b)–(f) *en face* projections of five distinctive layers (background subtraction in Fiji imageJ used to enhance contrast); (g) wide-field fluorescence image [green fluorescent protein (GFP) channel]; (h) superposition of (e) (in green) and (g) (in red). Scale bar: 100 μm.

for plaques, damaged neurons, and infectious agents. Thus, an increased number of the microglia cells near areas of increased scattering in the ELM might represent a local activation of these cells to the amoeboid state, allowing them to fulfill their role as scavenger cells. Clearly, further studies with fluorescent reporters expressed in other cells types and possibly images of microglia with higher resolution AO-based imaging systems will be needed to determine the nature of this pathology.[49] This result nonetheless provides an example of the potential power of *en face* intensity projections of the different retinal layers for fast phenotypic multimodal screening of experimental animals. Notably, these scattering structures are not readily seen in B-scans, because they do not have a distinctive cross-sectional profile. Rather, they provide another example, like the capillary beds of the OPL and IPL layers, in which distinctive scattering elements are visualized more readily as patterns in two-dimensional projections of segmented layers. It is worth mentioning that the major choroidal vessels are readily visualized in Fig. 5(f), even in this pigmented mouse. This image was generated by projecting all intensities below the lowest boundary [retinal pigment epithelium (RPE)/Bruch's membrane] in Fig. 5(a). Overall, segmentation of retinal layers from OCT volumetric data and *en face* projection provide an important tool for analysis of retinal features and discovery.

3.5 *Simultaneous Scanning Laser Ophthalmoscopy and Phase-Variance Optical Coherence Tomography Data Enable the Choroidal Vasculature to be Resolved in Nonpigmented Mice*

As described earlier, our OCT subsystem can operate in pv-OCT acquisition mode, which provides a label-free way to map the retinal vasculature. We used a nonpigmented nude (NU/NU) mouse to illustrate potential of the combined SLO/OCT system to perform retinal and choroidal angiography. Nude mice lack body hair and have a genetic mutation that causes a deteriorated or absent thymus, resulting in depressed immune function. They are widely used as a model of human tissue and tumor cell xenografts, as they lack the normal immune response to foreign cells. Nude mouse also lack RPE pigmentation, and as in other albino mice, this absence makes it very difficult to map the retinal vasculature with standard fluorescein angiography due to the high-fluorescence background from the choroidal vasculature.

A cocktail of green-fluorescing fluorescein and 30-nm micellar nanoparticles tagged with red-fluorescing rhodamine-X was injected to the tail vein of two nude mice (NU/NU). One of the mice was imaged with the combined SLO and pv-OCT, while the second was followed by emission spectroscopy over 48 h to measure the changes in fluorescence intensity in the retina of these two materials as a function of time after the tail vein injection.

Figure 6(a) shows the SLO reflectance image, while Fig. 6(b) is the image from the green/GFP fluorescence channel. In this latter image, retinal capillaries are not visible due to the severe contrast degradation of the fluorescence evoked from the posterior eye. Figure 6(c) shows the fluorescence image from the red/mCherry channel depicting the rhodamine-X fluorescence: This channel reveals vascular details not seen in the green channel. We hypothesize that the relative loss of contrast and detail in the green image arises because fluorescein molecules (MW 376) are much smaller than the nanoparticles, and thus much more readily leak out of the fenestrated choroidal vasculature. The red-to-green-ratio image [Fig. 6(d)] provides further enhanced visualization of both retinal and choroidal vessels. Definitive segregation of the retinal and choroidal vasculature was obtained with pv-OCT analysis. Figure 6(f) shows a pv-OCT B-scan corresponding to the intensity B-scan image of Fig. 6(e). Color-coded *en face* projections of the pv-OCT data from the anterior [upper band between green dashed lines in Fig. 6(f)] and posterior retina [lower band between blued dashed lines in Fig. 6(f)] exhibit completely different patterns: compare Fig. 6(g) and 6(h). We note that the major anterior blood vessels cause "shadows" that diminish the scattering signals arising from the more posterior retinal vessels. Angiography of the choroidal vasculature with SLO is not readily performed in pigmented mice, due to the light absorption of the RPE melanin (SLO angiography) and RPE scattering, but clearly can be performed with both modalities in nonpigmented mice and with

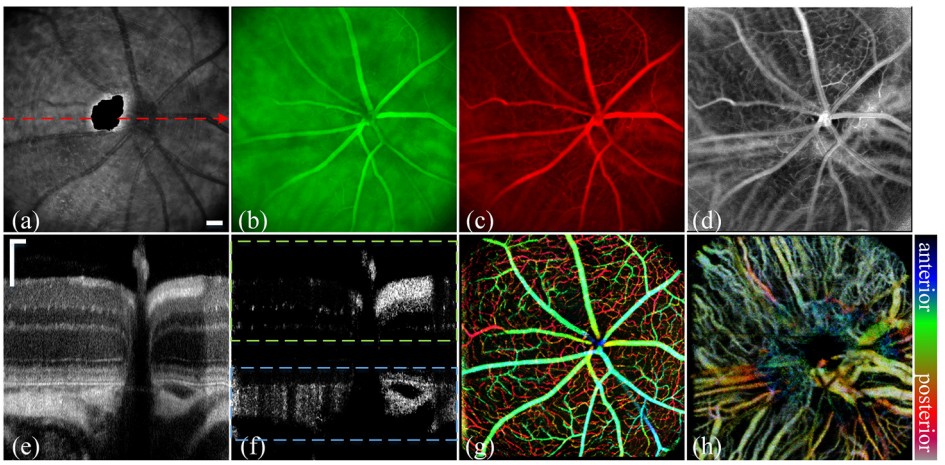

Fig. 6 Simultaneous SLO and pv-OCT imaging of a nude mouse injected with fluorescein and nanoparticles tagged with rhodamine-X: (a) SLO back-reflection image; (b) image of mid-wave ("GFP") fluorescence channel [Fig. 3(d)]; (c) image of long-wave fluorescence channel [Fig. 3(d)]; (d) image of ratio between (c) and (b); (e) OCT B-scan intensity-taken retinal location indicated by the red dashed arrow in (a); (f) pv-OCT B-scan image corresponding to (e), revealing areas of flow; (g) depth color-coded blood vessels and capillaries from NFL to OPL layer (green rectangle area in (f)); (h) depth color-coded choroid layer [blue rectangle area in (f)]. Note that (g) and (h) share the same color bar. Scale bar: 100 μm.

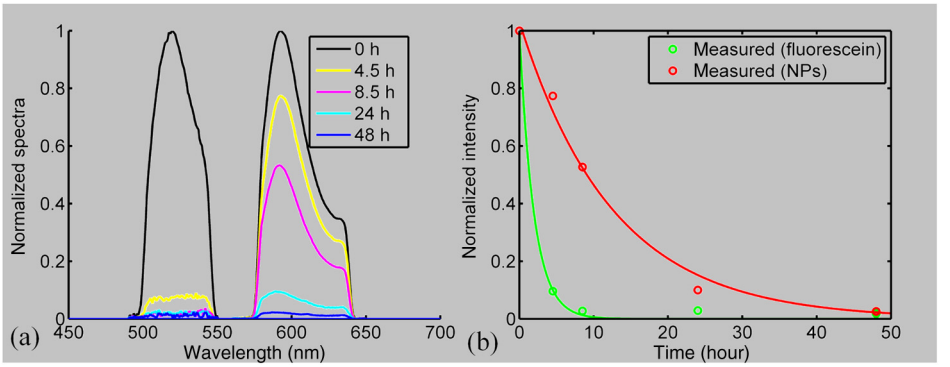

Fig. 7 Half-life measurement for fluorescein and rhodamine-X-tagged micellar nanoparticles (NPs): (a) average normalized fluorescence emission spectra (fluorescein: left side, rhodamine-X: right side) measured with a spectrometer from three distinct regions lacking major retinal vessels over time. (b) Normalized integration intensity changes of fluorescence emission spectra fitted with exponential functions ($\tau_{\text{fluoresciein}} = 1.4$ h, $\tau_{\text{NPs}} = 8.7$ h).

OCT in pigmented mice [Fig. 5(f)]. Use of the red-fluorescing nanoparticles clearly enhances choroidal fluorescence angiography, as can be seen by comparison of the red/green ratio image [Fig. 6(d)] with the simultaneously acquired pv-OCT data set [Fig. 6(h)]. This enhancement is thought to arise from both lower retinal tissue scattering and consequently better penetration of the longer wavelength light, and a lower rate of leakage of the 30-nm nanoparticles from the fenestrated choroidal vasculature.

As we have shown intravenously injected nanoparticles to be an efficient contrast agent for the choriodal vasculature (Fig. 6), we were interested in comparing the half-life of the retinal fluorescence of the nanoparticles with that of the more commonly used angiographic agent fluorescein. We used the spectrometer to measure the fluorescence emission over time after the tail vein injection, using the same excitation spectra and power level, and the same spectrometer integration time. Notably, because the pinhole size to airy disk ratio of spectrometer2 is twice as large as that of the fluorescence channels, it is relatively insensitive to the mouse positioning. Normalized emission spectra of the second nude mouse, simultaneously injected with both fluorochromes, are shown in Fig. 7(a). The results show that the fluorescein fluorescence was cleared much faster than that of the rhodamine-X-tagged nanoparticles: The time constant of the decay of the fluorescein was 1.4 h, while that of the rhodamine-X was 8.7 h, revealing a 6.2-fold shorter half-life for fluorescein in the vasculature.

4 Conclusions

OCT and SLO are two distinct retinal imaging modalities that provide different *in vivo* visualization of retinal morphology and function. Each modality has its distinctive advantages and limitations. By acquiring OCT and SLO data simultaneously, a wealth of complementary information can be obtained in a single imaging session.

4.1 *Advantages of Combined Optical Coherence Tomography and Scanning Laser Ophthalmoscopy Imaging*

Due to the use of a contact lens and the small diameter of the imaging beam, the monochromatic ocular aberrations of the mouse eye produce relatively little degradation in the acquired images. The axial shift of focus between OCT and SLO beams due to longitudinal (axial) chromatic aberrations and the lateral shift between two images are easily corrected by changing the divergence of the imaging beams and coregistering the two images, respectively. The three channels of our SLO system share the same light-delivery path with the OCT subsystem, and the data of both modalities are acquired simultaneously. Therefore, the acquired signals are automatically coregistered spatially and temporarily. Two examples were presented in this study. First, we investigated the colocalization of fluorescently labeled microglia as compared to elevated scattering observed by OCT in different retina layers. Second, we compared OCTA-generated blood perfusion maps with fluorescence-based angiography. In the first case, no definitive colocalization was observed. In the second case, we confirmed that our combined SLO/OCT system generates closely coregistered images, and that *en face* display of depth-encoded OCT data can provide new insights into the axial location of the signal that generates specific structures seen by SLO, as exemplified by retinal and choroidal vasculature.

We plan to use this system in the future to explore cellular (SLO) and morphological (OCT) correlations present during the development and progression of disease in mouse models of human eye diseases. We anticipate that some of the findings will be directly applicable to clinical imaging, allowing better diagnosis of disease progression in human subjects using OCT systems only. Additional study of clearance times and leakage from the vasculature of molecules and nanoparticles of different size in retina and choroid may greatly improve insight into the blood retina barrier, and its dependence on retinal health status.

4.2 *Limitations of Combined Scanning Laser Ophthalmoscopy and Optical Coherence Tomography Imaging in Mice*

The main limitations of our current instrument are the relatively slow acquisition speed of the OCT subsystem (100 kHz A-scan rate), which reduces overall acquisition speed and lack of optical magnification when scanning smaller ROIs. The first limitation can be easily overcome with next-generation high-acquisition speed OCT systems.[50,51] Overcoming the second limitation will require a different optical design, and most likely the application of adaptive optics.[7,8,49,52,53]

In summary, the SLO-OCT system affords the opportunity for rich analysis of automatically coregistered data of the two modalities. In particular, the capacity of the SLO for resolving a variety of different endogenous and exogenous fluorochromes (genetically encoded or transiently introduced) is a critical factor in this development. This will open the door to a better understanding of the signals from each modality, and thus of retinal structure and function *in vivo*.

Acknowledgments

We thank Dr. John S. Werner's VSRI Lab and Dr. Vivek J. Srinivasan in Biomedical Engineering Department of UC Davis for help and support. This research was supported by a UC Davis Research in Science and Engineering Grant, by NSF I/UCRC CBSS Grant, by NIH Grants EY24320 (MEB), EY02660 (ENP), EY012576 (NEI Core Grant), EB012569 (KSL).

References

1. M. W. Seeliger et al., "*In vivo* confocal imaging of the retina in animal models using scanning laser ophthalmoscopy," *Vision Res.* **45**(28), 3512–3519 (2005).
2. C. Alt et al., "*In vivo* tracking of hematopoietic cells in the retina of chimeric mice with a scanning laser ophthalmoscope," *IntraVital* **1**(2), 132–140 (2012).
3. G. Huber et al., "Spectral domain optical coherence tomography in mouse models of retinal degeneration," *Invest. Ophthalmol. Vis. Sci.* **50**(12), 5888–5895 (2009).
4. M. Ruggeri et al., "*In vivo* three-dimensional high-resolution imaging of rodent retina with spectral-domain optical coherence tomography," *Invest. Ophthalmol. Visual Sci.* **48**(4), 1808–1814 (2007).
5. O. P. Kocaoglu et al., "Simultaneous fundus imaging and optical coherence tomography of the mouse retina," *Invest. Ophthalmol. Visual Sci.* **48**(3), 1283–1289 (2007).
6. M. Paques et al., "High resolution fundus imaging by confocal scanning laser ophthalmoscopy in the mouse," *Vision Res.* **46**(8–9), 1336–1345 (2006).
7. Y. Jian et al., "Wavefront sensorless adaptive optics optical coherence tomography for *in vivo* retinal imaging in mice," *Biomed. Opt. Express* **5**(2), 547–559 (2014).
8. Y. Jian, R. J. Zawadzki, and M. V. Sarunic, "Adaptive optics optical coherence tomography for *in vivo* mouse retinal imaging," *J. Biomed. Opt.* **18**(5), 056007 (2013).
9. R. H. Webb and G. W. Hughes, "Scanning laser ophthalmoscope," *IEEE Trans. Biomed. Eng.* **BME-28**(7), 488–492 (1981).
10. P. F. Sharp et al., "The scanning laser ophthalmoscope—a review of its role in bioscience, and medicine," *Phys. Med. Biol.* **49**(7), 1085–1096 (2004).
11. D. Huang et al., "Optical coherence tomography," *Science* **254**(5035), 1178–1181 (1991).
12. A. F. Fercher et al., "Measurement of intraocular distances by backscattering spectral interferometry," *Opt. Commun.* **117**(1–2), 43–48 (1995).
13. M. Wojtkowski et al., "*In vivo* human retinal imaging by Fourier domain optical coherence tomography," *J. Biomed. Opt.* **7**(3), 457–463 (2002).
14. W. Drexler and J. G. Fujimoto, "State-of-the-art retinal optical coherence tomography," *Prog. Retinal Eye Res.* **27**(1), 45–88 (2008).
15. A. F. Fercher et al., "Optical coherence tomography—principles and applications," *Rep. Prog. Phys.* **66**(2), 239–303 (2003).
16. W. Song et al., "Integrating photoacoustic ophthalmoscopy with scanning laser ophthalmoscopy, optical coherence tomography, and fluorescein angiography for a multimodal retinal imaging platform," *J Biomed Opt.* **17**(6), 061206 (2012).
17. D. X. Hammer et al., "Multimodal adaptive optics retinal imager: design and performance," *J. Opt. Soc. Am. A* **29**(12), 2598–2607 (2012).
18. R. B. Rosen et al., "Simultaneous OCT/SLO/ICG Imaging," *Invest. Ophthalmol. Visual Sci.* **50**(2), 851–860 (2009).
19. C. K. Brinkmann, S. Wolf, and U. E. K. Wolf-Schnurrbusch, "Multimodal imaging in macular diagnostics: combined OCT-SLO improves therapeutical monitoring," *Graefe's Arch. Clin. Exp. Ophthalmol.* **246**(1), 9–16 (2008).
20. M. N. Menke et al., "Combined use of SLO microperimetry and OCT for retinal functional and structural testing," *Graefe's Arch. Clin. Exp. Ophthalmol.* **244**(5), 634–638 (2006).
21. K. Komar et al., "Multimodal instrument for high-sensitivity autofluorescence and spectral optical coherence tomography of the human eye fundus," *Biomed. Opt. Express* **4**(11), 2683–2695 (2013).
22. M. Mujat et al., "High resolution multimodal clinical ophthalmic imaging system," *Opt. Express* **18**(11), 11607–11621 (2010).
23. R. J. Zawadzki et al., "Integrated adaptive optics optical coherence tomography and adaptive optics scanning laser ophthalmoscope system for simultaneous cellular resolution *in vivo* retinal imaging," *Biomed. Opt. Express* **2**(6), 1674–1686 (2011).
24. Y. Geng et al., "Optical properties of the mouse eye," *Biomed. Opt. Express* **2**(4), 717–738 (2011).
25. M. A. Bermudez et al., "Time course of cold cataract development in anesthetized mice," *Curr. Eye Res.* **36**(3), 278–284 (2011).
26. A. Zam et al., "Evaluation of OCT for quantitative in-vivo measurements of changes in neural tissue scattering in longitudinal studies of retinal degeneration in mice," *Proc. SPIE* **8934**, 893422 (2014).
27. J. Fingler et al., "Mobility and transverse flow visualization using phase variance contrast with spectral domain optical coherence tomography," *Opt. Express* **15**(20), 12636–12653 (2007).
28. D. Y. Kim et al., "*In vivo* volumetric imaging of human retinal circulation with phase-variance optical coherence tomography," *Biomed. Opt. Express* **2**(6), 1504–1513 (2011).
29. D. Y. Kim et al., "Optical imaging of the chorioretinal vasculature in the living human eye," *PNAS* **110**(35), 14354–14359 (2013).
30. S. Makita et al., "Optical coherence angiography," *Opt. Express* **14**(17), 7821–7840 (2006).
31. R. K. Wang et al., "Three dimensional optical angiography," *Opt. Express* **15**(7), 4083–4097 (2007).
32. L. An and R. K. Wang, "*In vivo* volumetric imaging of vascular perfusion within human retina and choroids with optical micro-angiography," *Opt. Express* **16**(15), 11438–11452 (2008).
33. M. Szkulmowski et al., "Flow velocity estimation using joint spectral and time domain optical coherence tomography," *Opt. Express* **16**(9), 6008–6025 (2008).
34. A. Mariampillai et al., "Speckle variance detection of microvasculature using swept-source optical coherence tomography," *Opt. Lett.* **33**(13), 1530–1532 (2008).
35. E. Jonathan, J. Enfield, and M. J. Leahy, "Correlation mapping method for generating microcirculation morphology from optical coherence tomography (OCT) intensity images," *J. Biophotonics* **4**(9), 583–587 (2011).
36. Y. Jia et al., "Split-spectrum amplitude-decorrelation angiography with optical coherence tomography," *Opt. Express* **20**(4), 4710–4725 (2012).
37. Y. H. Zhao et al., "Phase-resolved optical coherence tomography and optical Doppler tomography for imaging blood flow in human skin with fast scanning speed and high velocity sensitivity," *Opt. Lett.* **25**(2), 114–116 (2000).
38. S. T. Bailey et al., "Improved visualization of choroidal neovascularization in age-related macular degeneration with optical coherence tomography angiography compared to fluorescein angiography," *Invest. Ophthalmol. Vis. Sci.* **55**(13), 255 (2014).
39. P. F. Zhang et al., "Evaluation of state-of-the-art imaging systems for *in vivo* monitoring of retinal structure in mice: current capabilities and limitations," *Proc. SPIE* **8930**, 893005 (2014).
40. R. J. Zawadzki et al., "Ultrahigh-resolution optical coherence tomography with monochromatic and chromatic aberration correction," *Opt. Express* **16**(11), 8126–8143 (2008).
41. P. Thevenaz, U. E. Ruttimann, and M. Unser, "A pyramid approach to subpixel registration based on intensity," *IEEE Trans. Image Process.* **7**(1), 27–41 (1998).
42. Y. P. Li et al., "Well-defined, reversible boronate crosslinked nanocarriers for targeted drug delivery in response to acidic pH values and cis-diols," *Angew. Chem* **51**(12), 2864–2869 (2012).
43. Y. P. Li et al., "Well-defined, reversible disulfide cross-linked micelles for on-demand paclitaxel delivery," *Biomaterials* **32**(27), 6633–6645 (2011).

44. Y. Li et al., "A smart and versatile theranostic nanomedicine platform based on nanoporphyrin," *Nat. Commun.* **5**, 4712 (2014).
45. P. P. Srinivasan et al., "Automatic segmentation of up to ten layer boundaries in SD-OCT images of the mouse retina with and without missing layers due to pathology," *Biomed. Opt. Express* **5**(2), 348–365 (2014).
46. B. J. Antony et al., "Automated 3D segmentation of intraretinal surfaces in SD-OCT volumes in normal and diabetic mice," *Trans. Vision Sci. Tech.* **3**(5), 8 (2014).
47. M. Paques et al., "Structural and hemodynamic analysis of the mouse retinal microcirculation," *Invest. Ophthalmol. Visual Sci.* **44**(11), 4960–4967 (2003).
48. Z. Zhi et al., "Noninvasive imaging of retinal morphology and microvasculature in obese mice using optical coherence tomography and optical microangiography," *Invest. Ophthalmol. Vision Sci.* **55**(2), 1024–1030 (2014).
49. R. J. Zawadzki et al., "Adaptive-optics SLO imaging combined with widefield OCT and SLO enables precise 3D localization of fluorescent cells in the mouse retina," *Biomed. Opt. Express* **6**(6), 2191–2210 (2015).
50. T. Klein et al., "Multi-MHz retinal OCT," *Biomed. Opt. Express* **4**(10), 1890–1908 (2013).
51. I. Grulkowski et al., "Retinal, anterior segment and full eye imaging using ultrahigh speed swept source OCT with vertical-cavity surface emitting lasers," *Biomed. Opt. Express* **3**(11), 2733–2751 (2012).
52. Y. Geng et al., "Adaptive optics retinal imaging in the living mouse eye," *Biomed. Opt. Express* **3**(4), 715–734 (2012).
53. D. P. Biss et al., "*In vivo* fluorescent imaging of the mouse retina using adaptive optics," *Opt. Lett.* **32**(6), 659–661 (2007).

Pengfei Zhang is a postdoctoral researcher at the University of California Davis. He received his BS, MS, and PhD degrees in optical engineering from the Xi'an Jiaotong University in 2004, 2007, and 2011, respectively. His current research interests include development and application of *in vivo* mouse retinal imaging systems (scanning laser ophthalmoscopy, optical coherence tomography and their combinations with adaptive optics) for studying structural and functional changes at cellular resolution in the living mouse.

Biographies for the other authors are not available.